JGR Atmospheres

RESEARCH ARTICLE
10.1029/2021JD036090

Transient Behavior of the Asian Summer Monsoon Anticyclone Associated With Eastward Eddy Shedding

Xinyue Wang[1,2], William Randel[2], Laura Pan[2], Yutian Wu[3], and Pengfei Zhang[4]

[1]National Center for Atmospheric Research, Advanced Study Program, Boulder, CO, USA, [2]Atmospheric Chemistry Observations and Modeling Lab, National Center for Atmospheric Research, Boulder, CO, USA, [3]Lamont-Doherty Earth Observatory of Columbia University, Palisades, NY, USA, [4]Department of Meteorology and Atmospheric Science, Pennsylvania State University, University Park, PA, USA

Key Points:

- Eastward eddy shedding from the Asian monsoon anticyclone is often associated with the emergence of an isolated western Pacific (WP) anticyclone
- WP anticyclone is closely related to the Silk Road pattern. Eddies grow along the jet associated with baroclinic heat fluxes
- Eastward eddy shedding occasionally occurs in association with the Pacific-Japan pattern forced by strong convection near the Philippines

Supporting Information:

Supporting Information may be found in the online version of this article.

Correspondence to:

X. Wang,
xinyuew@ucar.edu

Citation:

Wang, X., Randel, W., Pan, L., Wu, Y., & Zhang, P. (2022). Transient behavior of the Asian summer monsoon anticyclone associated with eastward eddy shedding. *Journal of Geophysical Research: Atmospheres*, *127*, e2021JD036090. https://doi.org/10.1029/2021JD036090

Received 28 OCT 2021
Accepted 18 MAR 2022

Author Contributions:

Conceptualization: Xinyue Wang, William Randel
Data curation: Xinyue Wang
Formal analysis: Xinyue Wang
Funding acquisition: Xinyue Wang
Investigation: Xinyue Wang
Methodology: Xinyue Wang, William Randel
Supervision: William Randel, Laura Pan
Visualization: Xinyue Wang
Writing – original draft: Xinyue Wang
Writing – review & editing: Xinyue Wang, William Randel, Laura Pan, Yutian Wu, Pengfei Zhang

Abstract The Asian monsoon anticyclone (AMA) exhibits a trimodal distribution of sub-vortices and the western Pacific is one of the preferred locations. Amplification of the western Pacific anticyclone (WPA) is often linked with eastward eddy shedding from the AMA, although the processes are not well understood. This study investigates the dynamics driving eastward eddy shedding associated with the emergence of the WPA in the upper troposphere and lower stratosphere on synoptic scales. Using reanalysis data during 1979–2019, our composite analysis reveals that amplified WPA events are tied to the upstream Silk Road (SR) wave-train pattern over midlatitude Eurasia as identified in previous studies. The quasi-stationary eastward propagating eddies result from baroclinic excitation along the westerly jet, as identified by coherent eddy heat fluxes and weakening of the low-level temperature gradient. The upper-level westerly jet is important in determining the longitudinal phase-locking of wave trains, which are anchored and amplify near the jet exit. Occasionally enhanced convection near the Philippines also triggers anticyclonic eddies that propagate upward and northeastward via the Pacific-Japan (PJ) pattern, forming the WPA in the upper troposphere. Correlation analysis suggests that the SR and PJ mechanisms are not physically correlated.

1. Introduction

The Asian monsoon anticyclone (AMA) is the major circulation pattern in the upper troposphere and lower stratosphere (UTLS) during Northern summer, covering large parts of Eurasia. Relatively high tropospheric trace gases (e.g., water vapor, carbon monoxide, and hydrogen cyanide) and aerosol (e.g., sulfate and black carbon) concentrations are confined within the area of anticyclonic circulation, imposing a substantial effect on UTLS composition, and also potentially on the surface weather and climate (Höpfner et al., 2019; Randel & Park, 2006; Randel et al., 2010, 2015; Santee et al., 2017; Solomon et al., 2011; Vernier et al., 2015; X.; Wang et al., 2018; Y.; Wu et al., 2020; Zheng et al., 2021).

Understanding the location and movement of the AMA is important for quantifying dynamical and trace gas evolution in the UTLS. Studying the behavior of AMA dates back to Tao and Zhu (1964) who found the opposite movement between the upper-level AMA and mid-level western North Pacific subtropical high in East Asia. Previous studies assuming the anticyclone has a single center reveal that the AMA exhibits a bimodal distribution over Iran and the Tibetan Plateau (TP) (Q. Zhang et al., 2002). The details of the bimodal distribution are sensitive to the use of different reanalysis data sets (Nützel et al., 2016), and bimodality is potentially driven by variations in convection (e.g., Garny & Randel, 2013), monsoonal heating (e.g., P. Zhang et al., 2016), orographic effects (Q. Zhang et al., 2002; Liu et al., 2007), and large-scale dynamical variability (Amemiya & Sato, 2020). More recent analyses have highlighted that the AMA is subject to large dynamical variability on synoptic scales, constantly splitting, merging, and shedding anticyclonic eddies westward and eastward (Garny & Randel, 2013, 2016; Manney et al., 2021; Pan et al., 2016; P. M. Rupp & Haynes, 2020). C. J. Hsu and Plumb (2000) showed that an idealized monsoon anticyclone circulation periodically sheds secondary anticyclones due to dynamical instabilities, and observational confirmation of eddy shedding was first shown in Popovic and Plumb (2001). Siu and Bowman (2020) showed that anticyclonic sub-vortices often occur within the AMA at the same time with similar strength. Therefore, consideration of only a single center of the AMA belies the importance of its transient nature and smears out important details.

Recently, Honomichl and Pan (2020) tracked multiple simultaneous maxima of the AMA and identified a third preferred center near 140°E, which is referred to as the WPA or the Bonin high (Enomoto, 2004; Enomoto

et al., 2003). Chemical species and low potential vorticity (PV) air within the AMA are shed eastward associated with the emergence of WPA (Clemens et al., 2021; Fujiwara et al., 2021; Honomichl & Pan, 2020; Vogel et al., 2014). The atmospheric composition and transport pathways associated with the WPA will be systematically investigated in the Asian Summer Monsoon Chemical and Climate Impact Project (ACCLIP) during July–August 2022 (https://www2.acom.ucar.edu/acclip).

While observational studies consistently highlight the chemical signature of the WPA, consensus is yet to be reached on the associated dynamics. This topic has a substantial history. Previous research has concluded that several different mechanisms can contribute to the enhancement of the WPA. For example, Tao and Zhu (1964) pointed out that the AMA moves in the opposite direction of the WP subtropical high at 500 hPa, modulated by the precipitation in east China. Enomoto et al. (2003) used the primitive-equation model in Hoskins and Rodwell (1995) to study the formation mechanism of the (time-averaged) Bonin high. Their model sensitivity analysis showed that the Bonin high disappears by removing the diabatic cooling over the Asian jet while it still exists at monthly timescale when removing the heating in the WP region. Thus, they emphasized the importance of the external Rossby wave source induced by the cooling due to the monsoon-forced descent over the eastern Mediterranean Sea. The wave disturbances along the Asian jet across Eurasia have since been recognized as the "Silk Road (SR) pattern". In fact, the WPA over Japan was already simulated in Hoskins and Rodwell (1995) but considered to be a model defect after validation against reanalysis data. Further, Enomoto (2004) conducted a composite analysis to study interannual variability of monthly mean stationary Rossby waves along the subtropical jet (including anticyclonic anomalies over Japan), emphasizing the role of an intensified jet in contributing to the eastward group velocity of stationary waves. Yasui and Watanabe (2010) used a dry atmospheric general circulation model and identified the SR pattern as a part of the circumglobal teleconnection. They performed a singular value decomposition (SVD) analysis for the diabatic heating and meridional wind anomalies, and concluded that the heating anomalies over the eastern Mediterranean are most responsible for the formation of the WPA, rather than cooling anomalies induced by the monsoon. P. Rupp and Haynes (2021) used a dry dynamical core model to simulate interactions of the Asian monsoon with baroclinic eddies on the westerly jet. They observed a transition from a steady circulation with westward eddy shedding to an unstable eastward eddy shedding state as the background meridional temperature gradient gradually increases. Their results imply that the WPA emerges in response to interaction between localized forcing by monsoon and the midlatitude baroclinic eddies.

Furthermore, Kosaka and Nakamura (2006) argued that the emergence of the Bonin high can be attributed to the WP convective heating, contradicting the conclusion of Enomoto et al. (2003). The teleconnection between the convective activity in the tropical WP and the upper-level anticyclone anomaly over Japan is called the "Pacific-Japan (PJ) pattern" (Nitta, 1987). R. Lu and Lin (2009) employed a baroclinic model and suggested that the latent heating released from the rainfall anomalies near the Philippine Sea facilitates the eastward wave propagation toward Japan and forms the WPA. Similarly, Ren et al. (2015) showed that the diabatic heating induced by enhanced rainfall over the South China Sea initiates the eastward extension of the AMA. In addition, Kosaka et al. (2009) applied the empirical orthogonal function on monthly mean 200 hPa meridional winds spanning over the Asian monsoon regions and indicated that the SR pattern and the PJ pattern coincide. Chen and Huang (2012) performed an SVD analysis between upper-level meridional wind across Asia and tropical rainfall on monthly timescales and identified that the SR pattern also includes a signature of the PJ pattern. Thus, the studies listed above have reached different conclusions, and our goals include revisiting these mechanisms in the context of transient WPA events. Moreover, the WPA has been mostly examined in the context of monthly and seasonal timescales, but the transient behavior of the WPA associated with eastward eddy shedding has not been fully analyzed.

A principal objective of this work is to examine the dynamical mechanisms of eastward eddy shedding associated with the formation of WPA, in particular for transient variability. Specifically, we aim to address the following questions: (a). How robust is the occurrence of WPA events in high temporal and spatial resolution data? (b). What are the drivers of the WPA events and what are the associated dynamical mechanisms? (c). What is the intraseasonal behavior of WPA events? Calculations are based on the latest high resolution reanalysis products from ERA5 (Section 2). In Section 3, we first analyze the statistical occurrence of enhanced Bonin high events and isolated large amplitude WPA, and their relationships to eastward eddy shedding. More specifically, we define a time-evolving Bonin High Index (BHI) to measure the strength of the ridge above the Bonin Islands,

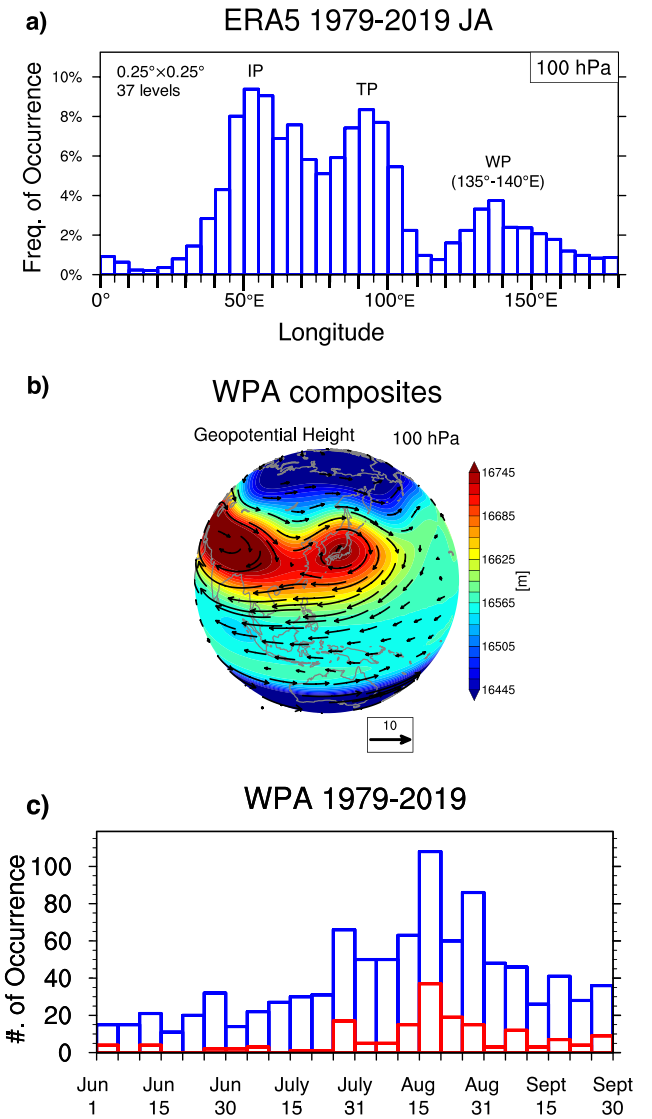

Figure 1. (a) The frequency distribution of the anticyclone centers versus longitude at 100 hPa compiled using ERA5 6-hourly geopotential during July–August 1979–2019 (2542 days in total). "IP" refers to the IP mode, "TP" refers to the TP mode, and "WP" refers to the western Pacific mode. (b) 100 hPa geopotential height (in colors, *m*) and horizontal circulation (in arrows, *m/s*) for composites associated with western Pacific anticyclone (WPA) events. (c) The distribution of WPA occurrence dates during June–September of 1979–2019. Blue bars indicate overall histograms while red bars indicate stronger anticyclonic events when the v wind threshold is 6 *m/s*.

select WPA events as closed anticyclone circulations, and analyze composite patterns to illustrate the time evolution of eastward shedding. Next, we construct the SR Index (SRI) and PJ Index (PJI) time series and quantify their relationships to WPA events. The dynamics of WPA are then investigated in relation to the SR and PJ patterns. The goal is to diagnose the synoptic-scale evolution of WPA events and their forcing mechanisms. Results are summarized and discussed in Section 4.

2. Reanalysis Data

We use European Centre for Medium-Range Weather Forecasts (ECMWF) ERA5 meteorological products (Hersbach et al., 2020), including geopotential (z), PV, zonal and meridional (u and v) wind fields, and temperature. We employ top net thermal radiation (the negative of outgoing longwave radiation, OLR) as a proxy for deep convection. Reanalyzes are used at 6-hourly intervals (0000, 0600, 1200, and 1800 UTC) with a horizontal resolution of 0.25° latitude × 0.25° longitude on 37 standard pressure levels. Our investigation focuses on the eastward eddy shedding at 100 hPa during the months of July–August over 41 years (1979–2019).

3. Results

3.1. Overview of the WPA

Several previous studies of the Asian summer anticyclone identified a single maximum along the geopotential ridge line and found a bimodal behavior, referred to as the TP mode and the Iranian Plateau (IP) mode (Nützel et al., 2016; Q. Zhang et al., 2002). Honomichl and Pan (2020) identified multiple simultaneous anticyclonic circulation centers at 100 hPa, and highlighted frequent occurrence of a third center over the WP. We follow their method to identify localized anticyclones, slightly modifying the details to eliminate any localized small-scale circulations in the higher resolution ERA5 data. Specifically, maxima are selected only if the meridional wind within 1500 km of the center along the ridge is greater than 3 *m/s* (−3 *m/s*) on the west (east) side. Note that we have adopted a more strict criterion (3 *m/s* vs. 0 *m/s* threshold as in Honomichl & Pan, 2020) for selecting local maxima due to the finer horizontal grid resolution of ERA5 than ERA-Interim. Figure 1a shows the histogram of frequency and longitude of transient anticyclone centers at 100 hPa for July–August. In addition to the IP mode near 50°E and TP mode near 90°E, a third preferred center is found over the WP peaking around 135°–140°E. The frequency distribution is almost identical to the previously calculated result (Figure 3a, Honomichl & Pan, 2020), and similar to the results of Siu and Bowman (2020). We have repeated the analysis on meteorological fields at 150 hPa level and found that the locations for the WPA remain the same (not shown).

To gain a better understanding of the dynamical processes leading to the eastward eddy shedding, we define the WPA event as an anticyclonic center that falls within the 135°-140°E longitudinal bin during July–August. Using 6-hourly ERA5 data over 41 years (1979–2019), we have identified ∼140 WPA events, that is, typically 3–4 events per year and most events have 3–4 days duration. The composite analysis shown in Figure 1a uses each synoptic time step of the events as a sample (total of 614 samples). Figure 1b shows the composited WPA geopotential height and associated winds that identify a separate anticyclone in the WP region, adjacent to the AMA. Figure 1c shows the number of WPA events during June to September of 1979–2019, showing that the occurrence of WPA peaks in late August and drops in September. Sensitivity test shows that doubling the v wind criterion to 6 *m/s*, that is, selecting stronger localized anticyclones, does not change the shape of the distribution

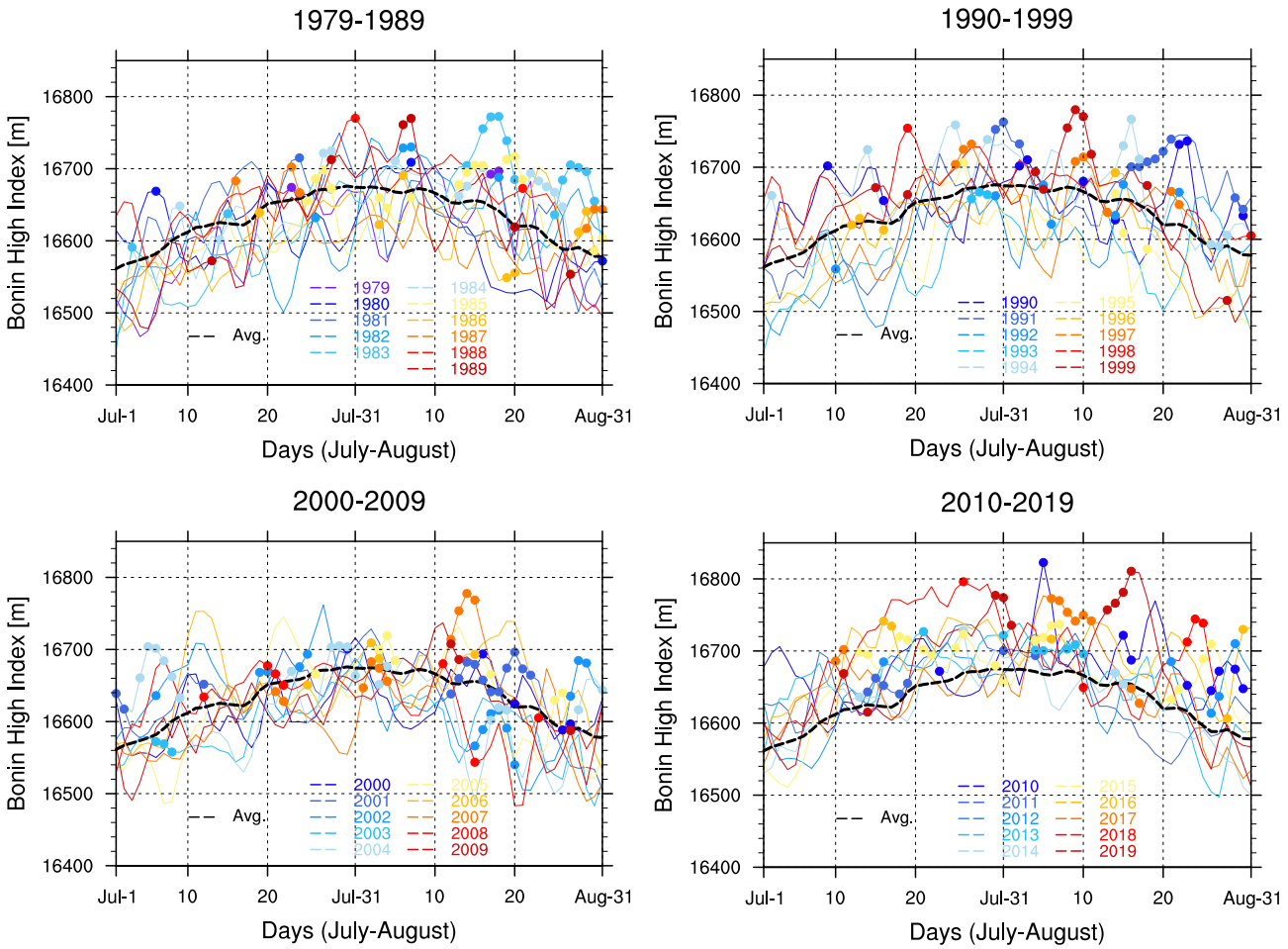

Figure 2. Time series of the Bonin High Index in July–August for each year 1979–2019 (in colors) and the 41-year average (black dashed curve). Colored dots indicate the identified western Pacific anticyclone events.

as indicated by red bars. We note that the distribution of anticyclonic centers for June–September is similar to that in Figure 1a (not shown), and the composited signals are about the same as for July–August.

To quantify the strength of the anticyclone over Japan, a BHI is defined as the regional averaged geopotential height within 30°–55°N and 135°–140°E. Figure 2 shows time series of the BHI during July and August 1979–2019 and the mean seasonal evolution, along with identified WPA events. The time series exhibit substantial intraseasonal and yearly variabilities in frequency and intensity. The intraseasonal evolution reveals that the Bonin high strength peaks in late July and slowly decays in August, largely corresponding to the variation in South Asian monsoon precipitation (Figure 3, Molnar et al., 2010). The recent decade has seen a general increase in BHI. Overall, the WPA events typically coincide with peaks in BHI, although not for all events. This is because we require the WPA to be an anticyclonic cell while the BHI does not indicate a closed contour, for example, a strong ridge can create large BHI values but not a WPA event.

The 100 hPa geopotential height and meridional wind anomalies composited for the WPA events are shown in Figures 3a and 3b, respectively. We subtract the climatological mean value for each time step to derive a deseasonalized anomaly. Here Day 0 denotes the first day of consecutive days showing a WPA event. The composited structure shows the WPA is embedded within a wave packet along the climatological westerly flow with an approximate zonal scale of wavenumber 6. Positive geopotential height coupled with intensified anticyclone occurs near the jet exit above Japan. The composite features are not sensitive to the choice of the longitude range in defining the WPA events (not shown). Temporal development of geopotential height averaged over 40°–45°N along the upper-level jet at 100 hPa is depicted by the Hovmöller diagram in Figure 3c, highlighting coherent

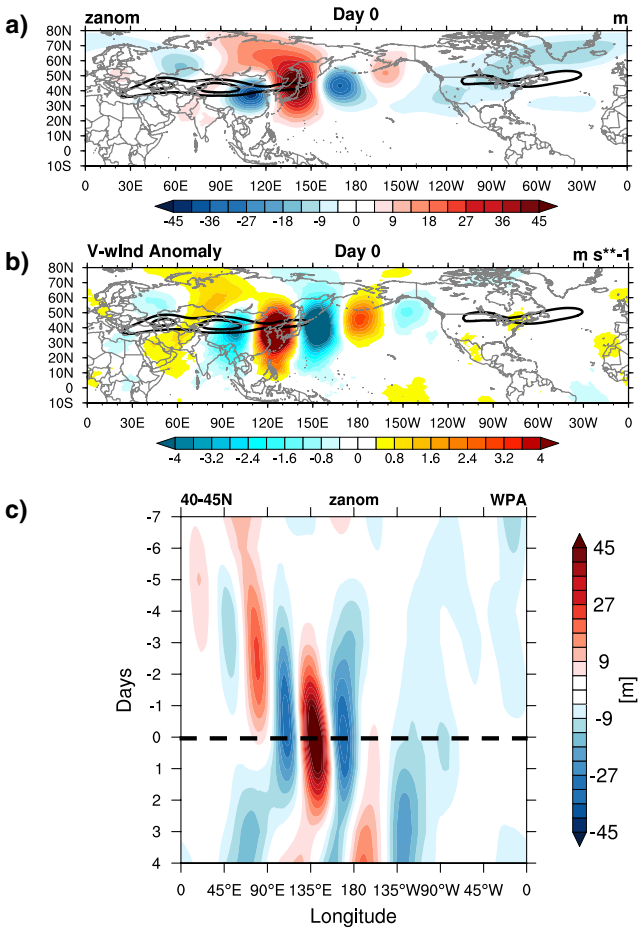

Figure 3. Composites of 100 hPa geopotential height and meridional wind anomalies (zanom and vanom) for the western Pacific anticyclone events on Day 0 in (a) and (b), respectively. Regions where anomalies are not significant at the 95% level using *t*-test are shaded white. Black contours highlight the 200 hPa climatological westerly jet of 24 and 30 *m/s*. (c) Hovmöller diagram of zanom at 100 hPa averaged over 40°–45°N from Day −7 to +4.

upstream wave structure beginning ~5 days prior to the WPA events. The wave packet has near zero phase speed, but a clear eastward group velocity near 24 *m/s*. The wave packet propagates downstream through the waveguide of the jet core, and amplifies near the jet exit on Day 0. The quasi-stationary zonal wavenumber 6 structure identified in Figure 3 is consistent with the SR behavior analyzed in Kosaka et al. (2009), interpreted as a stationary Rossby wave on the background westerly jet. Each WPA event can last for 3–4 days. During Day +1 to +4, wave packets develop successively downstream and reach the Pacific coast of the United States.

Figure 4a displays the time evolution of PV interpolated to 360 K isentropes for the composited WPA events. The anticyclone is associated with a region of relatively low PV, for example, Garny and Randel (2016) and Ploeger et al. (2017). Low PV patches develop on the eastern side of the anticyclone during the WPA events, in a manner consistent with wave trains seen in Figure 3. Figure 4b shows a Hovmöller diagram of PV at 360 K averaged over 35°-45°N from Day −7 to +4, highlighting development of low PV air over the composite WPA life cycle. During Day −4 to +2, the low PV air associated with the eastward shedding is confined between 120° and 150°E and remains quasi-stationary, consistent with the geopotential height signature in Figure 3. The PV evolution is consistent with the developing WPA transporting air masses with elevated mixing ratios of CO and H_2O rapidly into the extratropical lower stratosphere (Pan et al., 2016; Ploeger et al., 2015). We note that while the WPA is quasi-stationary, air parcel trajectories can move through the circulation and transport constituents toward the east, for example, Honomichl and Pan (2020), their Figure 7.

The composited WPA meteorological features include combined effects of the SR and PJ teleconnections-wave trains in the upper troposphere together with enhanced convection over the tropical WP (Figure S1). However, the SR and PJ patterns do not always coincide in individual cases, which motivates us to evaluate the WPA events in terms of relations to the SR and PJ indices and examine their dynamics separately.

3.2. WPA Relationships to the Silk Road Pattern

3.2.1. Defining a Silk Road Index

The most striking feature in Figure 3 is the quasi-stationary wave along the upper-level jet, resembling the SR pattern (Enomoto et al., 2003; R.-Y. Lu et al., 2002). To quantify the occurrence of the SR wave trains, we construct a time varying SR Index (SRI). As indicated by the composite map of geopotential height averaged over Day −4 to −1 preceding the WPA events in Figure 5, the SR pattern consists of four zonally oriented anomaly centers confined to 35°-55°N, located over **A** the Caspian Sea (40°-55°E), **B** central Asia (70°-85°E), **C** Mongolia (95°-115°E), and **D** east China (120°-140°E). Two negative geopotential height centers are marked as **A** and **C** while two positive centers are marked as **B** and **D**. We define za_i as the maximum geopotential height anomaly from climatology in box i and SRI is the sum of boxes **B** and **D** minus the sum of **A** and **C** as in Equation 1:

$$SRI = \sum_{i=A,C} -za_i + \sum_{i=B,D} za_i \quad (1)$$

Figure 6 shows a 2D distribution of SRI versus BHI for all daily samples over July–August 1979–2019. Contours represent the density of scatter points. There is a weak but statistically significant correlation in the distribution (r ~ 0.3), as expected from the results in Figure 3. The red dots in Figure 6 represent the WPA events, primarily falling in the upper right-hand quadrant, that is, large amplitude BHI and SRI. These statistics are consistent with an amplified SR pattern typically preceding the strong anticyclone above Japan by 1–4 days.

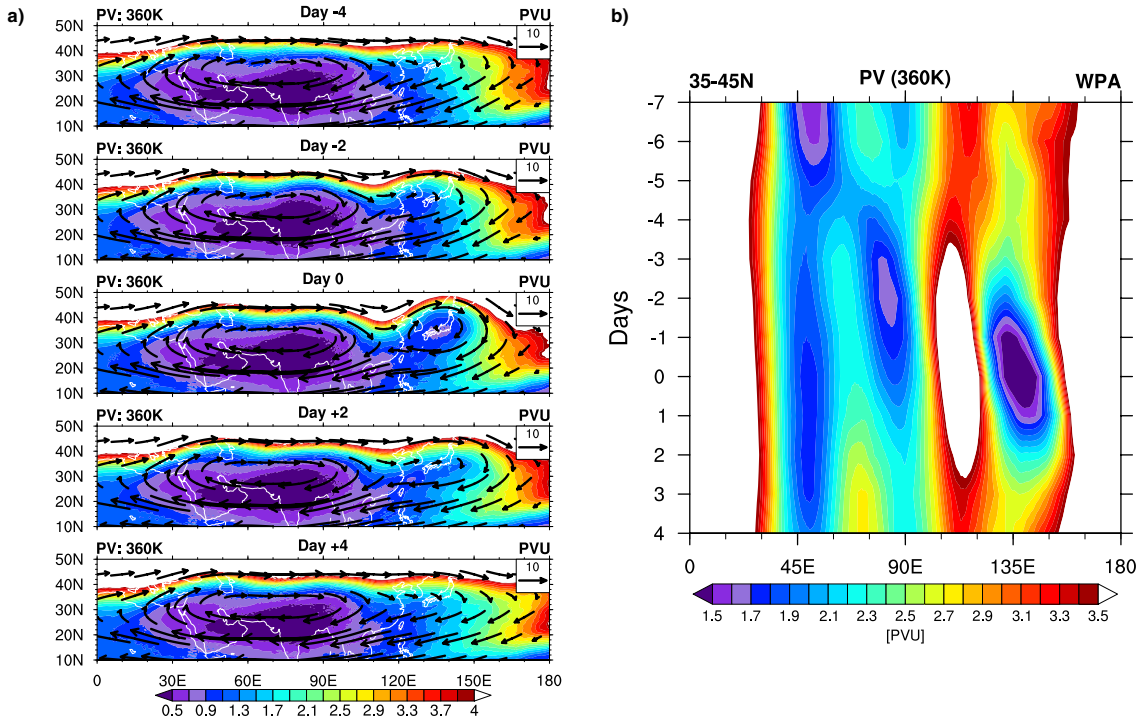

Figure 4. (a) Composite patterns of potential vorticity (PV) (in colors, PVU) at 360 K overlaid with the winds at 100 hPa (in vectors, m/s) on Day−4, Day−2, Day 0, Day +2, and Day +4 of the western Pacific anticyclone events, respectively. (b) Hovmöller diagram of PV at 360 K averaged over 35°-45°N from Day −7 to Day +4.

3.2.2. Dynamics in Relation to the Silk-Road Pattern

We apply composite analysis to obtain the essential circulation patterns of the WPA with reference to the intensity of the SR pattern. To sharpen the composited features, WPA events whose SRI fall above the 75th percentile are selected. Wave activity flux (WAF) vectors are computed to identify the origin and propagation of Rossby waves associated with the WPA events coinciding with the pronounced SR pattern. The calculation is based on the methods of Takaya and Nakamura (2001), which generalizes Plumb fluxes (Plumb, 1985) to allow for transient eddies propagating in a zonally varying mean state. The WAF is designed in the quasi-geostrophic (QG) framework, whose direction is parallel to the wave group velocity and the divergence (convergence) implies source (sink) of Rossby waves (Gu et al., 2018; H.-H. Hsu & Lin, 2007).

Figure 7a shows a latitude-height cross section of QG streamfunction anomalies and WAF averaged over 120°-140°E. Positive anomalous streamfunction around 150 hPa is equivalent to enhanced geopotential height fields, accompanying the upward flux from the lower troposphere near 40°-50°N above Japan, which is indicative of poleward eddy heat flux. Figure 7b is the meridional section over 40°-50°N, highlighting a train of high/low

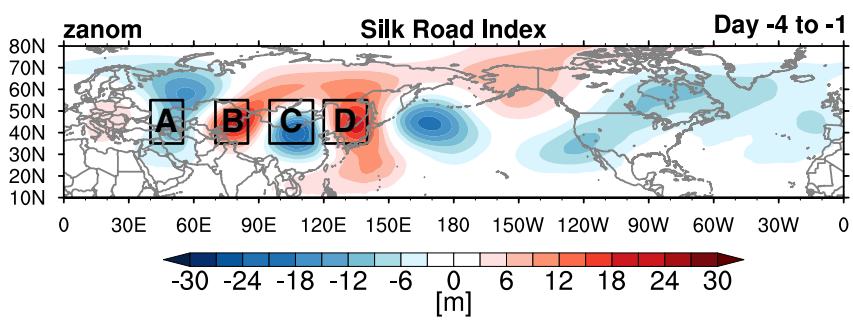

Figure 5. Schematic illustrating four centers where the SR Index is constructed. The zanom composites (in colors) are averaged during Day −4 to −1 prior to the western Pacific anticyclone events.

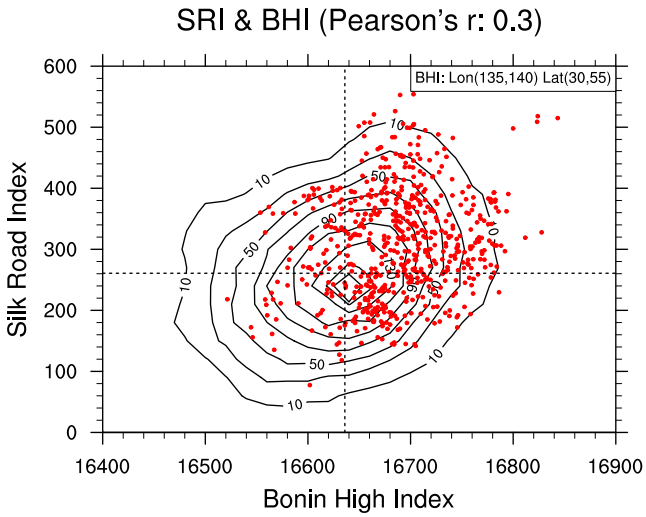

Figure 6. Two-dimensional distribution of the SR Index against the Bonin High Index compiled using all July–August data during 1979–2019. Red dots indicate the western Pacific anticyclone events. Dashed reference lines indicate the median values. Correlation coefficient is given in the figure title.

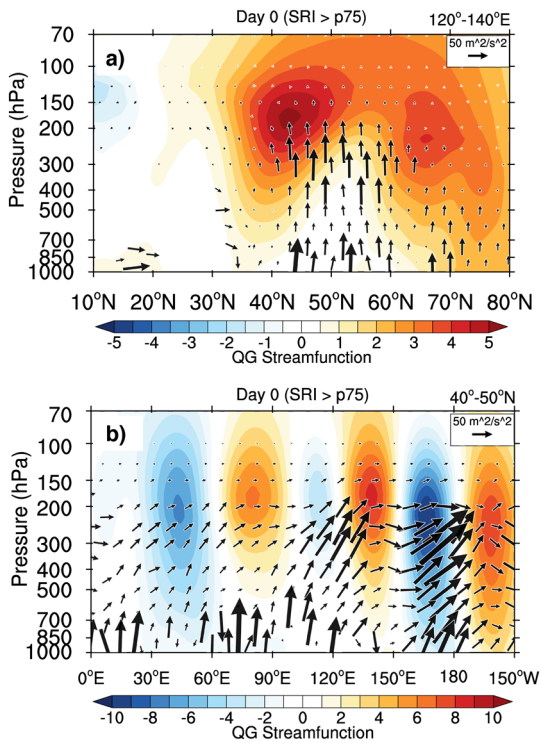

Figure 7. Cross sections of quasi-geostrophic streamfunction anomalies (in colors, unit: $10^{-6}\ m^2/s$) and Wave activity flux (in vectors, unit: m^2/s^2) (a) averaged over 120°-140°E and (b) at 40°N composited for the western Pacific anticyclone events which coincide with pronounced Silk Road pattern.

geopotential height anomaly centers in the upper troposphere with upward and eastward pointing WAF. This behavior is consistent with the eastward group velocity seen in Figure 3c.

The quasi-stationary zonal wavenumber 6 structure of the WPA/SR wave train is consistent with calculated stationary Rossby waves on the background westerly jet, which acts as a waveguide (Ding & Wang, 2005; Kosaka et al., 2009). The preferential phase locking of large WPA events, where the anticyclonic eddy maximum anchors near 135°–140°E rather than randomly moving around, may be related to the downstream end of the jet near these longitudes (Figure 3a). Geographically fixed anomaly patterns along a localized baroclinic jet have been discussed in Ambrizzi et al. (1995), Hoskins and Ambrizzi (1993), and H.-H. Hsu and Lin (1992). Background localized jet structure can also lead to amplification or over-reflection near the jet exit (Branstator, 1983; Hoskins & Ambrizzi, 1993), where the meridional gradient of absolute vorticity is close to zero (R. S. Lindzen & Tung, 1978). Calculations show that the meridional gradient of absolute vorticity at the jet exit is close to zero in 41-year climatology and also during the WPA events (not shown), supporting the possibility of wave over-reflection.

The wave activity fluxes in Figure 7a suggest close relationship with eddy heat fluxes ($\overline{v'T'}$, where bar and prime denote mean and deviation from temporal mean terms), signifying baroclinic wave growth. We further show the evolution of the vertically averaged eddy heat fluxes from 750 to 100 hPa in Figure 8. From Day −2 to −1, the northward eddy heat transport exhibits a strong local maximum over 90°–130°E and 30°–60°N slightly upstream of the WPA, suggesting an active role in amplifying the geopotential height anomaly downstream on Day 0. The heat fluxes gradually weaken and move northeastward on Day +1. The relationship to the composite WPA is quantified in Figure 9, showing a life cycle of BHI amplification lasting several days (cf. Figure 3c). Time variations in WPA composite $\overline{v'T'}$ shows a strong peak 1 day prior to the BHI maximum. The peak in baroclinic growth preceding the wave amplitude maximum is a signature of baroclinic forcing for the WPA events, and this behavior is similar to life cycles of idealized wavenumber-6 Rossby waves (Edmon Jr et al., 1980) and observations in the Southern Hemisphere (Randel & Stanford, 1985). In addition, Figure 9 shows a systematic reduction in the background temperature gradient ($-\frac{\partial T}{\partial y}$) from Day −3 to 0, coincident with wave growth and enhanced eddy heat flux. This coupled behavior is a clear signature of baroclinic wave growth, associated with heat transport down the mean temperature gradient which extracts available potential energy from the mean flow. These results are consistent with the findings of P. Rupp and Haynes (2021), who show that baroclinic eddies are intensified due to interaction with the northern edge of the anticyclone, leading to eastward eddy shedding (see their Figures 14c and 16).

3.3. WPA Relationships to the Pacific-Japan Pattern

3.3.1. Defining a Pacific-Japan Index

Composited OLR anomaly patterns for WPA events reveal that enhanced convection occurs over the tropical WP several days prior to the WPA events (Figure S1), which has been confirmed by the composites of precipitation anomalies (not shown). However, we find that this pattern is largely dominated by a few extreme events. As shown in Figure 10, the OLR anomalies in the vicinity of the Philippines and the South China Sea (10°–30°N, 130°–160°E) differ widely when the averaged OLR anomaly during day −6 to day −2 is below (Figure 10a) and above (Figure 10b) the 25th percentile of

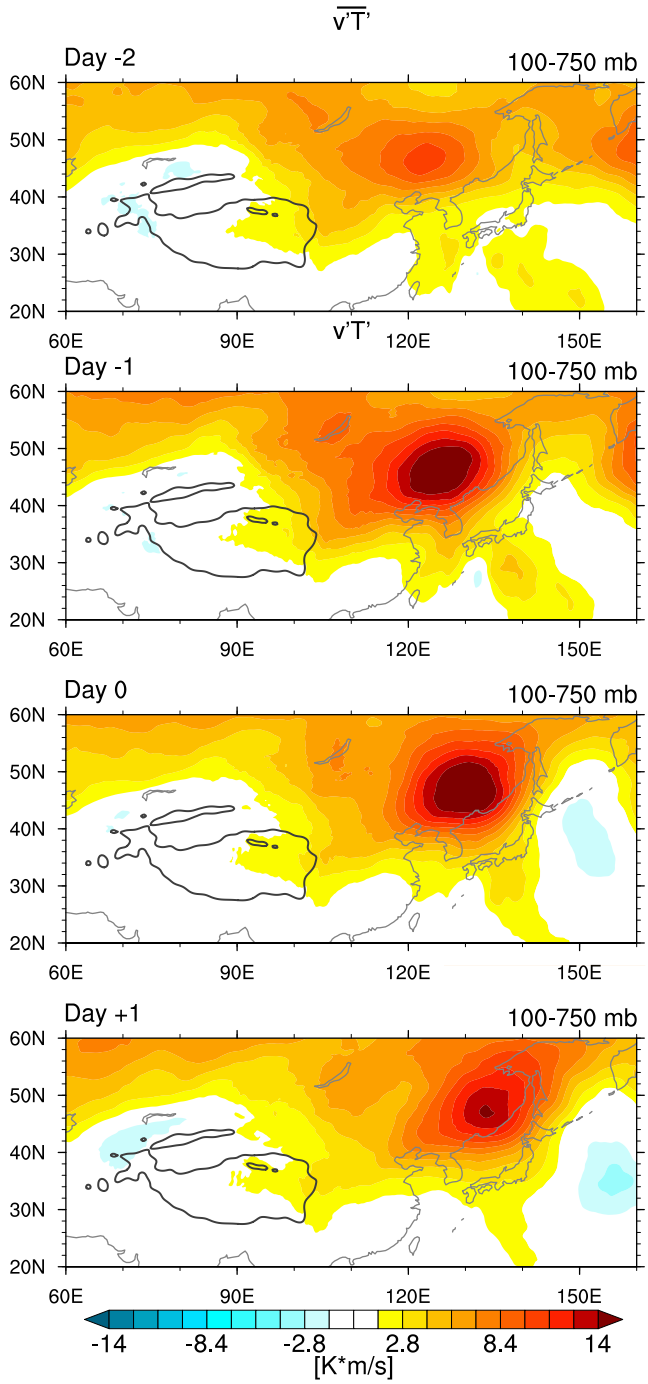

Figure 8. The vertically averaged eddy heat flux ($\overline{v'T'}$, *Km/s*) during Day −2 to +1 of the western Pacific anticyclone events. Black contours delineate the topographic boundary of 3,000 m.

the PJI index. Figure 10a displays a north-south tripole pattern, characterized by zonally elongated anomalies with signs changing alternatively from 0° to 45°N along the WP, signifying enhanced convective activity near 20°N sandwiched between two suppressed convection centers. This meridional teleconnection is referred to as the PJ pattern (Kosaka & Nakamura, 2006; H.-H.; Hsu & Lin, 2007; Kosaka et al., 2009; Kosaka & Nakamura, 2010; Nitta, 1987). However, the relation of OLR to WPA events disappears in composites for the upper 75% fraction (Figure 10b). This distinct contrast between Figures 10a and 10b demonstrates that a small fraction of the WPA events is associated with the PJ pattern while most of the cases are not.

The (negative) OLR anomaly averaged in the boxed region in Figure 10 during day −6 to −2 prior to the WPA events is used as the PJ Index (PJI)-the stronger convection around Philippines and the South China Sea, the lower OLR anomaly, and the larger PJI value corresponding to a more coherent PJ teleconnection pattern. Figure 11a shows the scatterplot between the PJI against BHI for the identified WPA events. Overall, the correlation is 0.27, which is weak but statistically significant. However, there is a stronger relationship for the strongest PJI values. For example, the red dots in Figure 11a represent the WPA events whose PJI falls above the 75th percentile and suggest a stronger positive correlation with the intensity of the WPA. Figure 11b shows the correlation coefficients between the PJI and the BHI for selected subsets of the data as the minimum PJI increases from −30, −20, …, 10, 15 W/m^2. The correlation is maximized when the PJI falls above the upper 30th percentile. The upper 30th percentile agrees well with statistics of back trajectories initialized within the WPA in Honomichl and Pan (2020), where one third of air parcels trace back to the Philippine Sea.

3.3.2. Dynamics in Relation to the Pacific-Japan Pattern

We apply composite analysis to identify the circulation patterns with reference to the intensity of the PJ pattern. Similar to Section 3.2.2, variables composited for the WPA events on Day 0 are averaged when the corresponding PJI falls above the 75th percentile, that is, enhanced convection as in Figure 10a (represented by gray contours in Figure 12b). Figure 12a shows the latitude-height cross section of QG streamfunction anomalies with WAF vectors averaged over 120°-140°E. Enhanced convection occurs near the Philippine Sea in accordance with negative zanom, triggering wave trains that propagate upward and poleward. Figure 12b exhibits that wave trains at 850 hPa originate from the south of Japan and reach the Gulf of Alaska roughly along an arc route, agreeing well with findings in previous studies (Figure 4 in R. Lu, 2004; Kosaka & Nakamura, 2006, 2010). Hoskins and Karoly (1981) provided an explanation for the great circle-like wave path using a baroclinic model. They have found that Rossby wave energy dispersion theory can describe the atmospheric activity at varying latitudes in a spherical atmosphere. The perturbation around 15°N initially moved northeastward, and then longer waves ($K_s \leq 3$) continued to propagate poleward while shorter waves were trapped by the northern flank of the jet and turned eastward. According to the ray tracing method (Equation 5.27 in Hoskins & Karoly, 1981), the turning latitude for tropical wavenumber 6 locates at around 45°N, consistent with the anomaly patterns shown in Figure 12b. In addition to the Rossby wave propagation mechanism, the extratropical transition of tropical cyclones (TC) can also result in the PJ wave trains. Amplified North Pacific flow develops following the TC recurvature, which is based on the negative PV advection by the divergent outflow of the TC (Archambault et al., 2013).

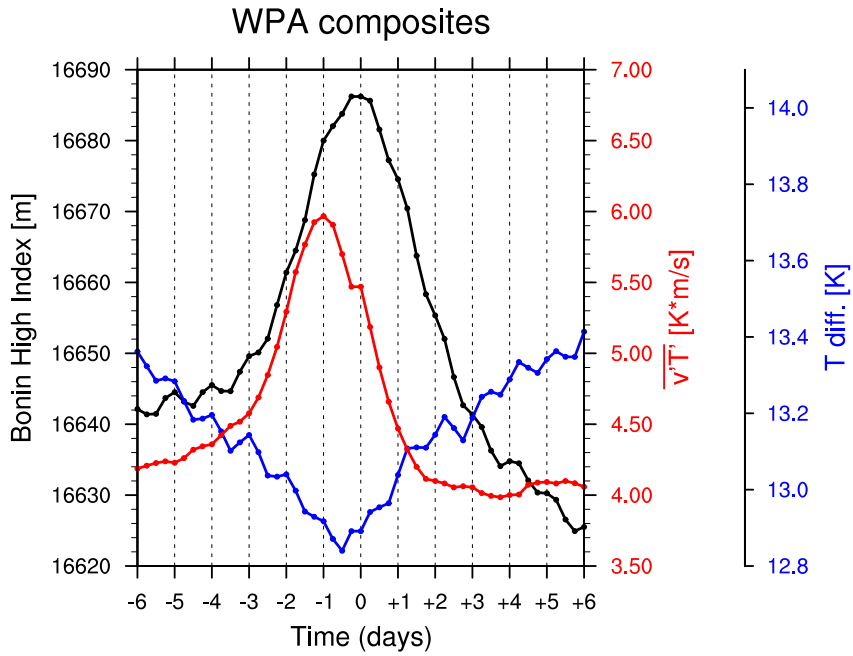

Figure 9. Life cycles of the composited western Pacific anticyclone (WPA)events in terms of BHI (black line), the vertically averaged heat flux (red line) over 90°-130°E and 30°-60°N, and the vertically averaged temperature difference between 30° and 60°N (blue line) over 90°-130°E from 300 to 550 hPa during Day −6 to +6 of the WPA events.

4. Discussion and Conclusion

The AMA exhibits a large spatial and temporal variability on the subseasonal scale. Using long-term ERA5 reanalysis products we have confirmed that the AMA forms a trimodal distribution in longitudes near 50°E (IP mode), 90°E (TP mode), and 135°E (WP mode) during July and August (Honomichl & Pan, 2020). The WP mode is associated with transient eddies that amplify as part of quasi-stationary wave trains, leading to a closed anticyclone over the Western Pacific with isolated low PV air. This work has focused on the dynamics driving the eastward eddy shedding associated with the presence of the WPA on synoptic timescales. While composited anomaly fields show combined influence of the SR and PJ patterns, these two teleconnections do not always coincide during the development of individual cases. Therefore, we categorized the WPA events into ones related to the SR and PJ mechanisms, respectively, and defined indices to quantify their features accordingly. The main results are summarized schematically in Figure 13.

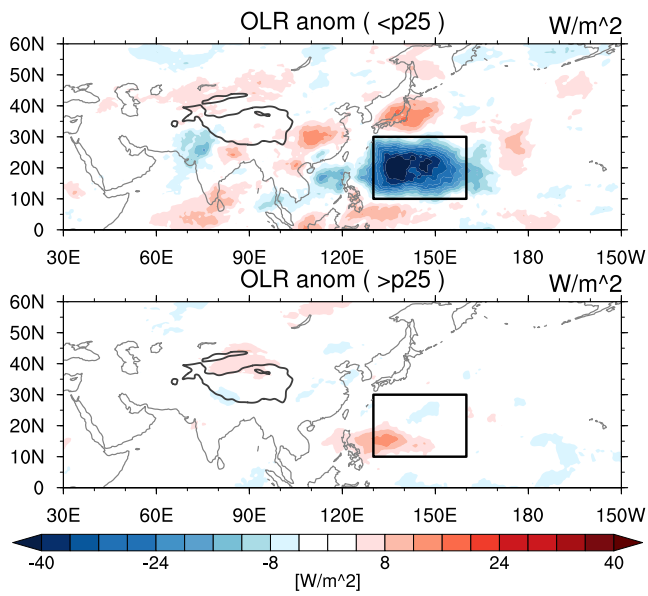

Figure 10. The composite maps of outgoing longwave radiation anomalies (W/m^2) during Day −6 to Day −2 prior to the western Pacific anticyclone events, separated according to the regional average over the boxed region (10°–30°N and 130°–160°E) falling (a) below and (b) above the 25th percentile of PJ Index. Black contours delineate the topographic boundary of 3,000 m.

First, the BHI is significantly correlated with the SRI, demonstrating that WPA events are closely tied with pronounced SR wave trains. The WPA amplitude growth is closely linked with systematic fluctuations in baroclinic wave forcing linked with eddy heat fluxes (Figures 8 and 9). The SR-related WPA reaches its largest amplitude 1 day after its maximum baroclinic growth, indicating anticyclonic eddies grow along the jet in response to the strong baroclinic background. We also find systematic weakening of the background temperature gradient throughout the WPA life cycles (Figure 9). These results are consistent with the model simulations reported by P. Rupp and Haynes (2021), in which they found that baroclinic eddies grow on the northern edge of the anticyclone with strong meridional temperature gradient, leading to eastward eddy shedding events. We furthermore estimated the seasonal cycle of the maximum growth rate of baroclinic instabilities given by R. Lindzen and Farrell (1980): $0.31\frac{g}{a\bar{T}N}|-\frac{\partial\bar{T}}{\partial\phi}|$, with $\bar{T}$ the vertically

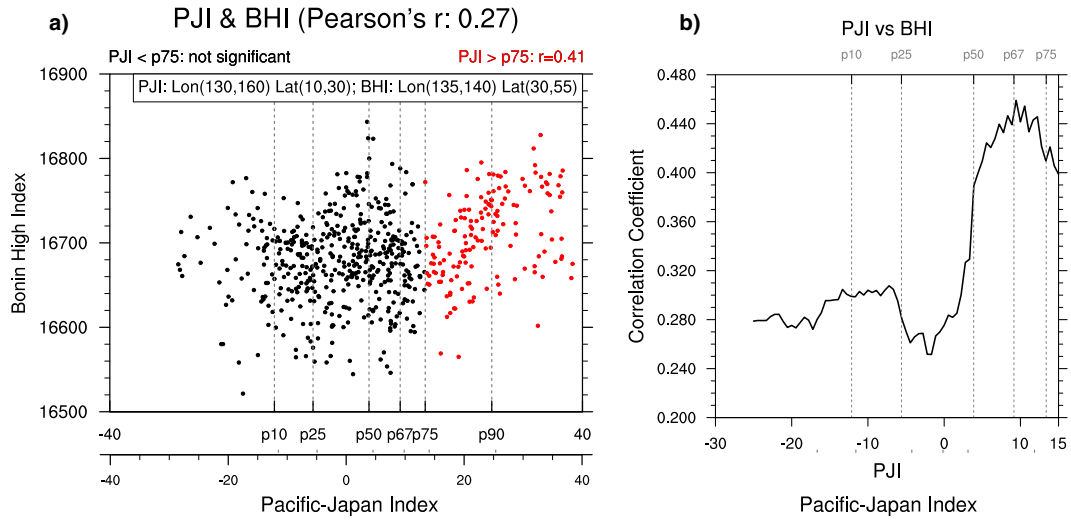

Figure 11. (a) Scatterplot between the Bonin High Index (BHI) (*m*) against the PJ Index (PJI) (W/m^2) composited for a total of 614 samples. Red dots highlight the Bonin high events whose PJI falls above the 75th percentile. Correlation coefficients are given in the figure title. Gray reference lines indicate the 10^{th} (p10), the 25th (p25), the median (p50), the 67th (p67), the 75th (p75), and the 90th (p90) percentiles of the PJI, respectively. (b) Correlation between subsets of the BHI and PJI, beginning at different minimum values of the PJI.

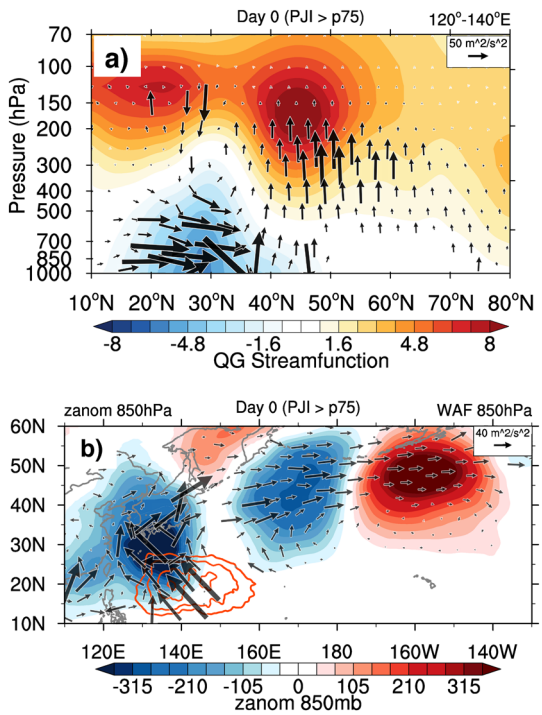

Figure 12. (a) Cross section of quasi-geostrophic streamfunction anomalies (in colors, unit: 10^{-6} m^2/s) and Wave activity flux (WAF) (in vectors, unit: m^2/s^2) averaged over 120°–140°E. (b) 850 hPa composited geopotential height anomalies (in colors) together with WAFs (in vectors, unit: m^2/s^2) for the western Pacific anticyclone events coinciding with the pronounced Pacific-Japan pattern. Orange contours represent negative outgoing longwave radiation anomaly centers (−50, −40, −30, …in W/m^2) as in Figure 10a.

averaged temperature; *a* the Earth radius; *g* the gravity acceleration; and *N* the Brunt-Väisälä frequency (not shown). The baroclinic instability along the midlatitude belt (30°–60°N, 0°–180°E) grows as the season progresses with correspondingly more WPA events in August (see Figure 1c), contributing to the seasonal variation in the WPA occurrence. While our results show clear links to dynamical structure, we do not find coherent changes in convective activity over the Bay of Bengal, the TP, and southern China prior to WPA growth (see Figure S1), implying that the eddies are not linked with convective forcings over the Indian summer monsoon region but rather with internal jet dynamics (Amemiya & Sato, 2020; Song et al., 2013; Sato & Takahashi, 2006). Although not shown, we have confirmed this finding by performing lag correlation between the BHI and multiple Indian summer monsoon indices (B. Wang & Fan, 1999), specifically, one convection index that characterizes the intensity change of the convective heating over the Bay of Bengal, as well as three circulation indices that quantify the Indian monsoon driven baroclinicity and the strength of the monsoon Hadley circulation over the Indian subcontinent. No significant correlation with the BHI can be identified among these indices based on the tropics from day −10 to 0, suggesting the limited role of monsoon convective forcings in exciting SR-related baroclinic eddies. As the eddies pass by the northern edge of the monsoon anticyclone, they interact with the PV minimum and the baroclinic wave structure gets further intensified (see Figure 3c).

Second, the correlation between the BHI and PJI suggests that about one third of the WPA events are associated with the PJ pattern. Composite analyses for the PJ-related WPA events show that perturbations originate in the lower troposphere due to convective forcing, radiating upward and maximizing in the UTLS region. Convective activities shift progressively northeastward from the Bay of Bengal to the western North Pacific from July to August (Figure 8 in B. Wang & Fan, 1999). The wet season peaks in late July over the northern Philippine and in August over the Philippine Sea (B. Wang, 1994). Meanwhile, typhoon activity peaks in August on the east of the Philippines

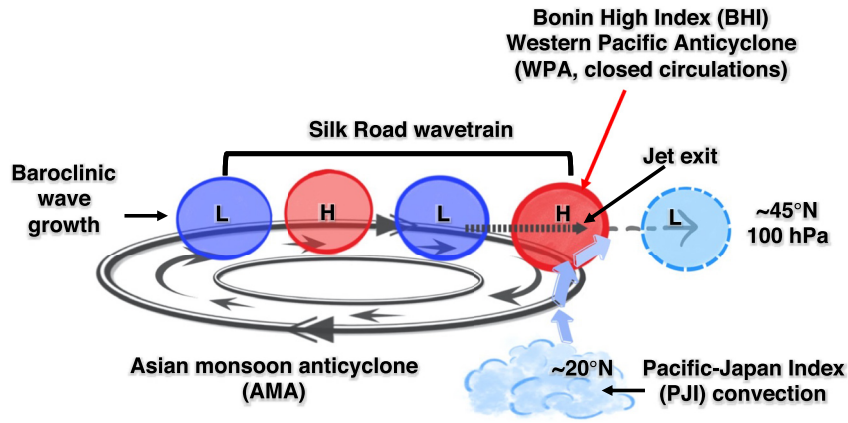

Figure 13. Schematic illustrating the dynamical mechanisms for the Bonin High and the western Pacific anticyclone events. The oval represents the climatology of the Asian monsoon anticyclone. "H" and "L" denote the centers of anticyclonic and cyclonic anomalies at 100 hPa. The thick dashed arrow indicates the location of upper-level jet exit while purple closed arrows indicate the direction of wave propagation associated with the P-J convection.

(L. Wu et al., 2014), resulting in more excitation of the PJ pattern (Kawamura & Ogasawara, 2006; Yamada & Kawamura, 2007). Consistent with this behavior, observations show that 70% of the PJ-related WPA events occur in August.

Previous studies have suggested that the monthly average SR pattern coexists with the PJ pattern (Chen & Huang, 2012; Kosaka et al., 2009). Here, we have found that the SRI is not significantly correlated with the PJI (not shown), suggesting that the SR and PJ mechanisms are physically independent processes. The two patterns coincide as a consequence of chance occurrence-enhanced convection in the tropical WP at the right time a SR wave train is traveling along. The monthly resolution used in previous studies is too coarse for differentiating the two processes. This is consistent with results in Sato and Takahashi (2006) that although the regression analysis shows the SR wave is correlated with the stronger convective activity over the WP, the divergent wind caused by the convection cannot excite the eastward propagating stationary Rossby wave coming from upstream.

Overall, we have addressed the following questions: (a). How robust is the occurrence of WPA events in high temporal and spatial resolution data? The WPA is statistically robust in the latest ERA5 6-hourly reanalysis at a quarter-degree resolution. The frequency distribution of WPA occurrences is not sensitive to the use of different horizontal resolution of reanalysis data. There are typically 3–4 events per summer. (b). What are the drivers of the WPA events and what are the associated dynamical mechanisms? While previous studies proposed that the Rossby wave excited by Indian summer monsoon diabatic heating anomaly is the major driver, from our analyses, it is the midlatitude baroclinic heat fluxes that is key forcing of the WPA. In response to the strong baroclinic background, eddies grow along the jet on the northern edge of the monsoon anticyclone, which is referred to as the SR pattern. The anticyclonic eddies amplify near the jet exit and form the WPA. Meanwhile, about one third of the WPA are substantially influenced by Philippines convection through the PJ mechanism. Anticyclonic eddies propagate upward and disperse eastward along the great circle as a consequence of strong rainfall and typhoons in the vicinity of the Philippines accompanied by weakening of the Indian summer monsoon. The two mechanisms are not significantly and physically correlated on synoptic scales. (c). What is the intraseasonal behavior of WPA events? The frequency of the WPA occurrence peaks in late August. More WPA events occur in August as a result of a combination of strong baroclinic instability on the northern edge of the AMA and the intensified (suppressed) Philippines (Bay of Bengal) convective activities. This work has synthesized previous studies and provided insights from dynamical perspectives for the design and implementation of the ACCLIP campaign.

An important issue not discussed in our paper is the potential link between westward and eastward eddy shedding activities. P. Rupp and Haynes (2021) observed a transition from a state with westward shedding to a state dominated by eastward shedding as the strength of the background flow varies. Our work has focused on eddies breaking off from the main anticyclone on the east side, and composited wave structure (e.g., Figure 3) does not

suggest any simple relationship with westward eddy shedding events. Whether a more subtle relationship exists between the two phenomena could be an interesting topic for future work.

Data Availability Statement

ERA5 meteorological products (ERA5, 2020) are available from the Copernicus Climate Data Store (https://cds.climate.copernicus.eu/cdsapp#!/dataset/reanalysis-era5-pressure-levels?tab=form).

Acknowledgments
Discussions with Philip Rupp and Peter Haynes provided valuable insights into this work. Comments by Shawn Honomichl, Warren Smith, Chris Davis, Na Wang, as well as careful reading by three anonymous reviewers led to substantial improvements in presentation. The authors appreciate the constructive discussion with the UTLS Group at the Atmospheric Chemistry Observations and Modeling, NCAR. We also acknowledge high-performance computing support from Brown Community Cluster provided by Purdue University. Xinyue Wang is supported by the NSF via the NCAR's Advanced Study Program Postdoctoral Fellowship. The NCAR is sponsored by the National Science Foundation.

References

Ambrizzi, T., Hoskins, B. J., & Hsu, H.-H. (1995). Rossby wave propagation and teleconnection patterns in the austral winter. *Journal of the Atmospheric Sciences*, *52*(21), 3661–3672. https://doi.org/10.1175/1520-0469(1995)052<3661:RWPATP>2.0.CO;2

Amemiya, A., & Sato, K. (2020). Characterizing quasi-biweekly variability of the Asian monsoon anticyclone using potential vorticity and large-scale geopotential height field. *Atmospheric Chemistry and Physics*, *20*(22), 13857–13876.

Archambault, H. M., Bosart, L. F., Keyser, D., & Cordeira, J. M. (2013). A climatological analysis of the extratropical flow response to recurving Western North Pacific tropical cyclones. *Monthly Weather Review*, *141*(7), 2325–2346. https://doi.org/10.1175/MWR-D-12-00257.1

Branstator, G. (1983). Horizontal energy propagation in a barotropic atmosphere with meridional and zonal structure. *Journal of the Atmospheric Sciences*, *40*(7), 1689–1708.

Chen, G., & Huang, R. (2012). Excitation mechanisms of the teleconnection patterns affecting the July precipitation in Northwest China. *Journal of Climate*, *25*(22), 7834–7851. https://doi.org/10.1175/JCLI-D-11-00684.1

Clemens, J., Ploeger, F., Konopka, P., Portmann, R., Sprenger, M., & Wernli, H. (2021). Characterization of transport from the Asian summer monsoon anticyclone into the UTLS via shedding of low-potential vorticity cutoffs. *Atmospheric Chemistry and Physics Discussions*, 1–32.

Ding, Q., & Wang, B. (2005). Circumglobal teleconnection in the Northern Hemisphere summer. *Journal of Climate*, *18*(17), 3483–3505. https://doi.org/10.1175/JCLI3473.1

Edmon, H., Jr, Hoskins, B., & McIntyre, M. (1980). Eliassen-Palm cross sections for the troposphere. *Journal of the Atmospheric Sciences*, *37*(12), 2600–2616.

Enomoto, T. (2004). Interannual variability of the Bonin high associated with the propagation of Rossby waves along the Asian jet. *Journal of the Meteorological Society of Japan. Ser. II*, *82*(4), 1019–1034. https://doi.org/10.2151/jmsj.2004.1019

Enomoto, T., Hoskins, B. J., & Matsuda, Y. (2003). The formation mechanism of the Bonin high in August. *Quarterly Journal of the Royal Meteorological Society: A journal of the atmospheric sciences, applied meteorology and physical oceanography*, *129*(587), 157–178. https://doi.org/10.1256/qj.01.211

ERA5. (2020). ERA5 hourly data on pressure levels from 1979 to present [Dataset]. ECMWF. https://doi.org/10.24381/cds.bd0915c6

Fujiwara, M., Sakai, T., Nagai, T., Shiraishi, K., Inai, Y., Khaykin, S., & Pan, L. L. (2021). Lower-stratospheric aerosol measurements in eastward-shedding vortices over Japan from the Asian summer monsoon anticyclone during the summer of 2018. *Atmospheric Chemistry and Physics*, *21*(4), 3073–3090.

Garny, H., & Randel, W. (2013). Dynamic variability of the Asian monsoon anticyclone observed in potential vorticity and correlations with tracer distributions. *Journal of Geophysical Research: Atmospheres*, *118*(24), 13–421. https://doi.org/10.1002/2013JD020908

Garny, H., & Randel, W. J. (2016). Transport pathways from the Asian monsoon anticyclone to the stratosphere. *Atmospheric Chemistry and Physics*, *16*(4), 2703–2718.

Gu, S., Zhang, Y., Wu, Q., & Yang, X.-Q. (2018). The linkage between arctic sea ice and midlatitude weather: In the perspective of energy. *Journal of Geophysical Research: Atmospheres*, *123*(20), 11–536. https://doi.org/10.1029/2018JD028743

Hersbach, H., Bell, B., Berrisford, P., Hirahara, S., Horányi, A., Muñoz-Sabater, J., et al. (2020). The ERA5 global reanalysis. *Quarterly Journal of the Royal Meteorological Society*, *146*(730), 1999–2049. https://doi.org/10.1002/qj.3803

Honomichl, S. B., & Pan, L. L. (2020). Transport from the Asian summer monsoon anticyclone over the Western Pacific. *Journal of Geophysical Research: Atmospheres*, *125*(13), e2019JD032094. https://doi.org/10.1029/2019JD032094

Höpfner, M., Ungermann, J., Borrmann, S., Wagner, R., Spang, R., Riese, M., et al. (2019). Ammonium nitrate particles formed in upper troposphere from ground ammonia sources during Asian monsoons. *Nature Geoscience*, *12*(8), 608–612.

Hoskins, B. J., & Ambrizzi, T. (1993). Rossby wave propagation on a realistic longitudinally varying flow. *Journal of the Atmospheric Sciences*, *50*(12), 1661–1671. https://doi.org/10.1175/1520-0469(1993)050<1661:RWPOAR>2.0.CO;2

Hoskins, B. J., & Karoly, D. J. (1981). The steady linear response of a spherical atmosphere to thermal and orographic forcing. *Journal of the Atmospheric Sciences*, *38*(6), 1179–1196.

Hoskins, B. J., & Rodwell, M. J. (1995). A model of the Asian summer monsoon. Part I: The global scale. *Journal of the Atmospheric Sciences*, *52*(9), 1329–1340.

Hsu, C. J., & Plumb, R. A. (2000). Nonaxisymmetric thermally driven circulations and upper-tropospheric monsoon dynamics. *Journal of the Atmospheric Sciences*, *57*(9), 1255–1276.

Hsu, H.-H., & Lin, S.-H. (1992). Global teleconnections in the 250-mb streamfunction field during the Northern Hemisphere winter. *Monthly Weather Review*, *120*(7), 1169–1190.

Hsu, H.-H., & Lin, S.-M. (2007). Asymmetry of the tripole rainfall pattern during the East Asian summer. *Journal of Climate*, *20*(17), 4443–4458. https://doi.org/10.1175/JCLI4246.1

Kawamura, R., & Ogasawara, T. (2006). On the role of typhoons in generating PJ teleconnection patterns over the Western North Pacific in late summer. *Solanus*, *2*, 37–40. https://doi.org/10.2151/sola.2006-010

Kosaka, Y., & Nakamura, H. (2006). Structure and dynamics of the summertime Pacific–Japan teleconnection pattern. *Quarterly Journal of the Royal Meteorological Society: A journal of the atmospheric sciences, applied meteorology and physical oceanography*, *132*(619), 2009–2030. https://doi.org/10.1256/qj.05.204

Kosaka, Y., & Nakamura, H. (2010). Mechanisms of meridional teleconnection observed between a summer monsoon system and a subtropical anticyclone. Part I: The Pacific–Japan pattern. *Journal of Climate*, *23*(19), 5085–5108. https://doi.org/10.1175/2010JCLI3413.1

Kosaka, Y., Nakamura, H., Watanabe, M., & Kimoto, M. (2009). Analysis on the dynamics of a wave-like teleconnection pattern along the summertime Asian jet based on a reanalysis dataset and climate model simulations. *Journal of the Meteorological Society of Japan. Ser. II*, *87*(3), 561–580. https://doi.org/10.2151/jmsj.87.561

Lindzen, R., & Farrell, B. (1980). A simple approximate result for the maximum growth rate of baroclinic instabilities. *Journal of the Atmospheric Sciences*, *37*(7), 1648–1654.
Lindzen, R. S., & Tung, K. (1978). Wave overreflection and shear instability. *Journal of the Atmospheric Sciences*, *35*(9), 1626–1632.
Liu, Y., Hoskins, B., & Blackburn, M. (2007). Impact of Tibetan orography and heating on the summer flow over Asia. *Journal of the Meteorological Society of Japan. Ser. II*, *85*, 1–19. https://doi.org/10.2151/jmsj.85B.1
Lu, R. (2004). Associations among the components of the East Asian summer monsoon system in the meridional direction. *Journal of the Meteorological Society of Japan. Ser. II*, *82*(1), 155–165. https://doi.org/10.2151/jmsj.82.155
Lu, R., & Lin, Z. (2009). Role of subtropical precipitation anomalies in maintaining the summertime meridional teleconnection over the Western North Pacific and East Asia. *Journal of Climate*, *22*(8), 2058–2072. https://doi.org/10.1175/2008JCLI2444.1
Lu, R.-Y., Oh, J.-H., & Kim, B.-J. (2002). A teleconnection pattern in upper-level meridional wind over the North African and Eurasian continent in summer. *Tellus A: Dynamic Meteorology and Oceanography*, *54*(1), 44–55. https://doi.org/10.3402/tellusa.v54i1.12122
Manney, G. L., Santee, M. L., Lawrence, Z. D., Wargan, K., & Schwartz, M. J. (2021). A moments view of climatology and variability of the Asian summer monsoon anticyclone. *Journal of Climate*, *34*(19), 7821–7841. https://doi.org/10.1175/JCLI-D-20-0729.1
Molnar, P., Boos, W. R., & Battisti, D. S. (2010). Orographic controls on climate and paleoclimate of Asia: Thermal and mechanical roles for the Tibetan Plateau. *Annual Review of Earth and Planetary Sciences*, *38*, 77–102. https://doi.org/10.1146/annurev-earth-040809-152456
Nitta, T. (1987). Convective activities in the tropical western Pacific and their impact on the Northern Hemisphere summer circulation. *Journal of the Meteorological Society of Japan. Ser. II*, *65*(3), 373–390.
Nützel, M., Dameris, M., & Garny, H. (2016). Movement, drivers and bimodality of the South Asian high. *Atmospheric Chemistry and Physics*(16), 14755–14774.
Pan, L. L., Honomichl, S. B., Kinnison, D. E., Abalos, M., Randel, W. J., Bergman, J. W., & Bian, J. (2016). Transport of chemical tracers from the boundary layer to stratosphere associated with the dynamics of the Asian summer monsoon. *Journal of Geophysical Research: Atmospheres*, *121*(23). https://doi.org/10.1002/2016JD025616
Ploeger, F., Gottschling, C., Griessbach, S., Grooß, J.-U., Guenther, G., & Konopka, P. (2015). A potential vorticity-based determination of the transport barrier in the Asian summer monsoon anticyclone. *Atmospheric Chemistry and Physics*, *15*(22), 13145–13159.
Ploeger, F., Konopka, P., Walker, K., & Riese, M. (2017). Quantifying pollution transport from the Asian monsoon anticyclone into the lower stratosphere. *Atmospheric Chemistry and Physics*, *17*(11), 7055.
Plumb, R. A. (1985). On the three-dimensional propagation of stationary waves. *Journal of the Atmospheric Sciences*, *42*(3), 217–229.
Popovic, J. M., & Plumb, R. A. (2001). Eddy shedding from the upper-tropospheric Asian monsoon anticyclone. *Journal of the Atmospheric Sciences*, *58*(1), 93–104.
Randel, W. J., & Park, M. (2006). Deep convective influence on the Asian summer monsoon anticyclone and associated tracer variability observed with Atmospheric Infrared Sounder (AIRS). *Journal of Geophysical Research: Atmospheres*, *111*(D12). https://doi.org/10.1029/2005JD006490
Randel, W. J., Park, M., Emmons, L., Kinnison, D., Bernath, P., Walker, K. A., & Pumphrey, H. (2010). Asian monsoon transport of pollution to the stratosphere. *Science*, *328*(5978), 611–613. https://doi.org/10.1126/science.1182274
Randel, W. J., & Stanford, J. L. (1985). The observed life cycle of a baroclinic instability. *Journal of the Atmospheric Sciences*, *42*(13), 1364–1373.
Randel, W. J., Zhang, K., & Fu, R. (2015). What controls stratospheric water vapor in the NH summer monsoon regions? *Journal of Geophysical Research: Atmospheres*, *120*(15), 7988–8001. https://doi.org/10.1002/2015JD023622
Ren, X., Yang, D., & Yang, X.-Q. (2015). Characteristics and mechanisms of the subseasonal eastward extension of the South Asian high. *Journal of Climate*, *28*(17), 6799–6822. https://doi.org/10.1175/JCLI-D-14-00682.1
Rupp, P., & Haynes, P. (2021). Zonal scale and temporal variability of the Asian monsoon anticyclone in an idealised numerical model. *Weather and Climate Dynamics Discussions*, 1–31.
Rupp, P. M., & Haynes, P. H. (2020). Spatio-temporal stability analysis applied to monsoon anticyclone flow. *Quarterly Journal of the Royal Meteorological Society*, *146*(729), 1861–1879. https://doi.org/10.1002/qj.3771
Santee, M., Manney, G., Livesey, N., Schwartz, M., Neu, J., & Read, W. (2017). A comprehensive overview of the climatological composition of the Asian summer monsoon anticyclone based on 10 years of Aura Microwave Limb Sounder measurements. *Journal of Geophysical Research: Atmospheres*, *122*(10), 5491–5514. https://doi.org/10.1002/2016JD026408
Sato, N., & Takahashi, M. (2006). Dynamical processes related to the appearance of quasi-stationary waves on the subtropical jet in the midsummer Northern Hemisphere. *Journal of Climate*, *19*(8), 1531–1544. https://doi.org/10.1175/JCLI3697.1
Siu, L. W., & Bowman, K. P. (2020). Unsteady vortex behavior in the Asian monsoon anticyclone. *Journal of the Atmospheric Sciences*, *77*(12), 4067–4088. https://doi.org/10.1175/JAS-D-19-0349.1
Solomon, S., Daniel, J. S., Neely, R. R., Vernier, J.-P., Dutton, E. G., & Thomason, L. W. (2011). The persistently variable "background" stratospheric aerosol layer and global climate change. *Science*, *333*(6044), 866–870. https://doi.org/10.1126/science.1206027
Song, F., Zhou, T., & Wang, L. (2013). Two modes of the Silk Road pattern and their interannual variability simulated by LASG/IAP AGCM SAMIL2. 0. *Advances in Atmospheric Sciences*, *30*(3), 908–921.
Takaya, K., & Nakamura, H. (2001). A formulation of a phase-independent wave-activity flux for stationary and migratory quasigeostrophic eddies on a zonally varying basic flow. *Journal of the Atmospheric Sciences*, *58*(6), 608–627.
Tao, S. T., & Zhu, F. (1964). The 100 mb flow patterns in southern Asia in summer and its relation to the advance and retreat of the West-Pacific subtropical anticyclone over the Far East. *Acta Meteorologica Sinica*, *34*(4), 385–396.
Vernier, J.-P., Fairlie, T., Natarajan, M., Wienhold, F., Bian, J., Martinsson, B., & Bedka, K. (2015). Increase in upper tropospheric and lower stratospheric aerosol levels and its potential connection with Asian pollution. *Journal of Geophysical Research: Atmospheres*, *120*(4), 1608–1619. https://doi.org/10.1002/2014JD022372
Vogel, B., Günther, G., Müller, R., Grooß, J., Hoor, P., Krämer, M., & Riese, M. (2014). Fast transport from Southeast Asia boundary layer sources to northern Europe: Rapid uplift in typhoons and eastward eddy shedding of the Asian monsoon anticyclone. *Atmospheric Chemistry and Physics*, *14*(23), 12–745.
Wang, B. (1994). Climatic regimes of tropical convection and rainfall. *Journal of Climate*, 1109–1118.
Wang, B., & Fan, Z. (1999). Choice of South Asian summer monsoon indices. *Bulletin of the American Meteorological Society*, *80*(4), 629–638.
Wang, X., Wu, Y., Tung, W., Richter, J. H., Glanville, A. A., Tilmes, S., & Kinnison, D. E. (2018). The simulation of stratospheric water vapor over the Asian summer monsoon in CESM1 (WACCM) models. *Journal of Geophysical Research: Atmospheres*, *123*(20), 11–377. https://doi.org/10.1029/2018JD028971
Wu, L., Chou, C., Chen, C.-T., Huang, R., Knutson, T. R., Sirutis, J. J., & Feng, Y.-C. (2014). Simulations of the present and late-twenty-first-century Western North Pacific tropical cyclone activity using a regional model. *Journal of Climate*, *27*(9), 3405–3424. https://doi.org/10.1175/JCLI-D-12-00830.1

Wu, Y., Orbe, C., Tilmes, S., Abalos, M., & Wang, X. (2020). Fast transport pathways into the Northern Hemisphere upper troposphere and lower stratosphere during northern summer. *Journal of Geophysical Research: Atmospheres*, *125*(3), e2019JD031552. https://doi.org/10.1029/2019JD031552

Yamada, K., & Kawamura, R. (2007). Dynamical link between typhoon activity and the PJ teleconnection pattern from early summer to autumn as revealed by the JRA-25 reanalysis. *SOLA*, *3*, 65–68. https://doi.org/10.2151/sola.2007-017

Yasui, S., & Watanabe, M. (2010). Forcing processes of the summertime circumglobal teleconnection pattern in a dry AGCM. *Journal of Climate*, *23*(8), 2093–2114. https://doi.org/10.1175/2009JCLI3323.1

Zhang, P., Liu, Y., & He, B. (2016). Impact of East Asian summer monsoon heating on the interannual variation of the South Asian high. *Journal of Climate*, *29*(1), 159–173. https://doi.org/10.1175/JCLI-D-15-0118.1

Zhang, Q., Wu, G., & Qian, Y. (2002). The bimodality of the 100 hPa South Asia High and its relationship to the climate anomaly over East Asia in summer. *Journal of the Meteorological Society of Japan. Ser. II*, *80*(4), 733–744.

Zheng, C., Wu, Y., Ting, M., Orbe, C., Wang, X., & Tilmes, S. (2021). Summertime transport pathways from different Northern Hemisphere regions into the Arctic. *Journal of Geophysical Research: Atmospheres*, *126*(4), e2020JD033811. https://doi.org/10.1029/2020JD033811